AgileSAR: Achieving Wide-Swath Spaceborne SAR Based on Time-Space Sampling

ZE YU[1], (Member, IEEE), **WENJIAO CHEN**[1], **PENG XIAO**[2], **AND CHUNSHENG LI**[1]

[1]School of Electronics and Information Engineering, Beihang University, Beijing 100083, China
[2]Qian Xuesen Laboratory of Space Technology, Department of Applied Science and Frontier Technology, Beijing 100094, China

Corresponding author: Chunsheng Li (chunshengli201@163.com)

ABSTRACT High resolution and wide swath, which are related to imaging quality and observation efficiency, are the key specifications for spaceborne synthetic aperture radar (SAR). Owing to the restrictions of the Nyquist sampling theorem, it is difficult to improve both specifications simultaneously. The increase of the swath width often leads to the decrease of the spatial resolution, e.g., in scanning SAR and terrain observation with progressive scan SAR. For a sparse scene, an image containing only a few targets has massive data but little useful information. This paper proposes a novel SAR observation mode, AgileSAR, which is based on the time–space sampling method and can overcome the limitations of the Nyquist theorem. It also increases the swath width while preserving the resolution of the sparse scene. AgileSAR steers the antenna beam towards a different sub-swath, generally after one or two pulse intervals, and the average pulse repetition rate corresponding to every sub-swath is much lower than that determined by the Nyquist theorem. Compared with Sentinel-1, which can achieve 5-m resolution and 80-km swath, a single azimuth-channel AgileSAR system can achieve 5-m resolution and 300-km swath for a sparse scene, once the corresponding system parameters are designed. The l_1 relaxation method is used to reconstruct sparse SAR images, and the reconstruction performance is quantitatively analyzed based on the estimation error. The simulation results validating the proposed method with sub-Nyquist samples can achieve approximately similar performance as conventional SAR with Nyquist samples.

INDEX TERMS Synthetic aperture radar, sparse, time-space sampling, estimation error, wide swath.

I. INTRODUCTION

SAR transmits pulses and receives echoes from the target region at the rate of the pulse repetition frequency (PRF). For conventional SAR imaging, PRF should satisfy the Nyquist sampling theorem and be higher than the instantaneous Doppler bandwidth [1], [2]. If not, the azimuth spectrum of the echo would be aliased, and the azimuth ambiguity would be a serious challenge [1], [2]. In addition, the echo must be completely received within one pulse repetition interval, i.e., the reciprocal of PRF, such that an increase of the swath width often leads to a decrease in the spatial resolution for conventional SAR. However, the backscattering of most targets in the target area observed by SAR is so weak that such an area is considered to be sparse for the extraction of strong scattering information [3], [4]. Therefore, the imaging result corresponding to the area can be reconstructed from an appropriately undersampled SAR echo according to the compressive sensing (CS) theory. Under the assumption of a sparse scene, this study will achieve a wide swath while preserving the resolution using the sub-Nyquist sampling method.

Research on sub-Nyquist sampling has been conducted for several decades and has attracted renewed attention since the CS theory is proposed. Sub-Nyquist sampling is applied in numerous fields and relieves the strain on the analog-to-digital converter (ADC) and storage media as the amounts of data keep increasing. From the perspective of conducting or omitting waveform modulation before sampling at a rate below Nyquist, the existing sampling methods can be divided into two categories. In the first, the input signal is modulated by a random or periodic waveform, and then sampling is conducted at a lower rate. It is adopted by single-pixel cameras [5]–[7], random demodulators [8], and modulated wideband converters (MWCs) [9]–[11]. A MWC is also applied on the range dimension by lower rate ADC in SAR systems [12]. In the other category, sampling is conducted directly at low rate without pre-processing.

It includes multi-coset sampling [13], [14], random equivalent sampling (RES) [15]–[17], randomly choosing sub-Nyquist samples from the already receiving Nyquist samples [18] or non-uniformly transmitting a smaller number of pulses [12] on the azimuth dimension in the SAR system.

To achieve the wide swath SAR system without the loss of resolution, sub-Nyquist sampling should be adopted on the azimuth dimension. Because the SAR system has no source of generating modulation, the first category of sub-Nyquist sampling method is not applicable on the azimuth dimension in SAR systems. Multi-coset sampling and RES, among the second category, are not applicable to achieve the wider width SAR system, because the former is equal to sample at a Nyquist rate and the latter may lead to conflict between the transmitting and receiving in the SAR system. Only the concept of the sub-Nyquist sampling on the azimuth dimension in SAR system was presented, which puts on one sub-swath to process [12], [18]. The practical sampling mechanism to widen the swath is not proposed, as available space-time resources are wasted.

This paper proposes a new SAR observation mode, Agile-SAR, which achieves a much wider swath without the loss of resolution for sparse scenes. SAR data acquisition can be regarded as the sampling of scene information in the space domain and the azimuth time domain. AgileSAR adopts a sparse sampling method applied for SAR by comparing with other sub-Nyquist sampling methods. It can achieve better reconstructed performance, i.e., in terms of mean square error. Fig. 1 illustrates the strip mapping mode and AgileSAR mapping mode. As shown in Fig. 1(b), AgileSAR allocates N_{Nyquist} consecutive Nyquist pulses for Q sub-swaths. The observed order of sub-swath is random, and the beam is steered towards the corresponding sub-swath. Compared with the conventional strip mapping mode in Fig. 1(a), Agile-SAR modifies the sampling in the space–time domain and increases the total swath width to Q times that of the strip mapping system, while the span of the Doppler frequency shift for targets in every sub-swath is unchanged and the resolution is preserved.

The paper is structured as follows. Section II adopts the l_1 optimization method to reconstruct the azimuth signal using sub-Nyquist samples. Simultaneously, it fits the statistical distribution of a scene backscattering cross-section with an ocean having several ships as an example, and quantitatively estimates the SAR image reconstruction performance under this prior distribution. Section III proposes the pseudo-random sub-Nyquist sampling method according to the reconstruction performance, and qualitatively proves that this sampling method can achieve optimal performance. Based on the pseudo-random sub-Nyquist sampling method, a novel time–space sampling method to increase the swath width with unchanged resolution for a sparse scene is proposed, and the corresponding observed method named as AgileSAR is introduced in Section IV. This section also overviews the process of SAR focusing and compares it with the reconstruction performance of conventional SAR.
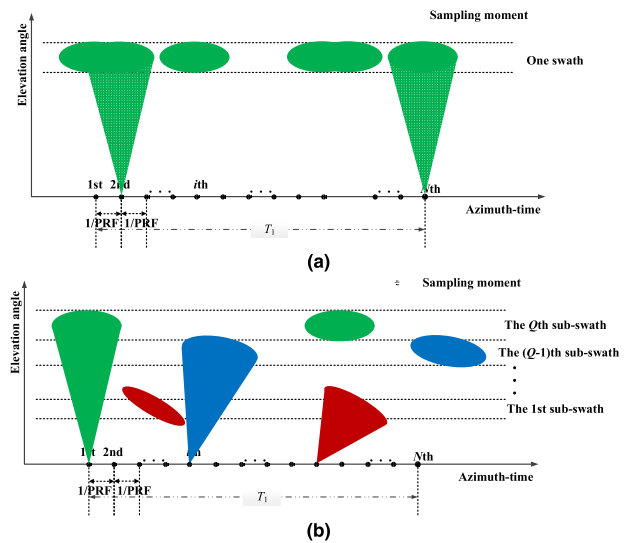

FIGURE 1. Illustration of time–space sampling. Each dot on the azimuth-time axis denotes one sample. (a) shows the conventional SAR sampling. The swath is sampled by the rate of PRF in the azimuth direction. The accumulated time is T_1, which is determined by the azimuth resolution. (b) shows the proposed time–space sampling. Q consecutive pulses are randomly allocated to Q sub-swaths. The beam needs to be steered towards the corresponding sub-swath. For each sub-swath, the sampling rate is much smaller than PRF, and the accumulated time is approximately T_1, which lays the foundation for preserving the azimuth resolution. In addition, sub-swaths except the Qth sub-swath with the largest incidence angle in Q sub-swaths should be squinted in the azimuth direction observed to guarantee echo completely received during the beam position design.

The design example of AgileSAR and simulation results are presented in Section V. Section VI concludes the paper.

II. SAR IMAGE RECONSTRUCTION BASED ON CS

Usually, spaceborne SAR is assumed to remain stationary while transmitting one pulse and receiving the corresponding echo before moving to the next position [1], [2]. Under this assumption, the echo from M point targets on the same nearest slant range can be modelled as follows:

$$
\begin{aligned}
s_0(\tau, \eta) = &\sum_{m=1}^{M} \sigma_m W_m(\tau, \eta)\, rect\left\{ \left(\tau - \frac{2R_m(\eta)}{c} \right) \Big/ T_r \right\} \\
&\cdot \exp\left\{ j\pi K_r \left[\tau - \frac{2R_m(\eta)}{c} \right]^2 - j4\pi \frac{R_m(\eta)}{\lambda} \right\} \\
&+ n(\tau, \eta),
\end{aligned}
\tag{1}
$$

where τ denotes the fast time in the range direction, and η represents the slow time in the azimuth direction. σ_m and $W_m(\tau, \eta)$ are the backscattering cross-section and the weighting factor of the mth point target, respectively. K_r denotes the frequency modulation rate of the pulse. $R_m(\eta)$ represents the distance between the radar and the mth point target at η. T_r is the pulse width. c is the light speed, and λ is the wavelength. $n(\tau, \eta)$ denotes the noise.

After range compression and range cell migration correction, the signal is given by the following:

$$
\begin{aligned}
s_c(\tau, \eta) &= \sum_{m=1}^{M} \sigma_m W_m(\tau, \eta) T_r \cdot \mathrm{sinc}\left\{ K_r T_r \left[\tau - \frac{2R_m\left(\eta_{c_m}\right)}{c} \right] \right\} \\
&\quad \cdot \exp\left\{ -\frac{j4\pi R_m(\eta)}{\lambda} \right\} + n(\tau, \eta),
\end{aligned} \tag{2}
$$

where η_{c_m} is the beam centre crossing time for the mth target.

Equation (2) at many azimuth sampling instants can also be expressed as a vector-matrix form as follows:

$$
\mathbf{s}_{N \times 1} = \begin{bmatrix} s_c(\tau, \eta_1) \\ s_c(\tau, \eta_2) \\ \vdots \\ s_c(\tau, \eta_n) \\ \vdots \\ s_c(\tau, \eta_N) \end{bmatrix}_{N \times 1} = \mathbf{D}_{N \times M} \boldsymbol{\sigma}_{M \times 1} + \mathbf{n}_{N \times 1}, \tag{3}
$$

where

$$
\mathbf{n}_{N \times 1} = [n(\tau, \eta_1), n(\tau, \eta_2), \cdots, n(\tau, \eta_N)]^T,
$$
$$
\boldsymbol{\sigma}_{M \times 1} = [\sigma_1, \sigma_2, \cdots, \sigma_M]^T, \quad \mathbf{D}_{N \times M} = \{D_{nm}\}_{n=1, m=1}^{N, M},
$$
$$
D_{nm} = W_m(\tau, \eta_n) \cdot T_r \cdot \mathrm{sinc}\left\{ K_r T_r \left[\tau - \frac{2R_m\left(\eta_{c_m}\right)}{c} \right] \right\}
$$
$$
\cdot \exp\left[-j4\pi R_m(\eta_n)/\lambda \right] \},
$$

and N is the number of samples in the azimuth direction.

When the number of columns in the matrix $\mathbf{D}_{N \times M}$ is more than the number of rows, and the reconstructed vector $\boldsymbol{\sigma}_{M \times 1}$ is sparse, i.e., most elements of $\boldsymbol{\sigma}_{M \times 1}$ are zero or very small, $\boldsymbol{\sigma}_{M \times 1}$ can be reconstructed by adopting the appropriate algorithms under a certain condition. A typical l_1 regularization formulation [19] as follows:

$$
\widehat{\boldsymbol{\sigma}} = \min_{\sigma} \left\{ \|\mathbf{s}_{N \times 1} - \mathbf{D}_{N \times M} \boldsymbol{\sigma}_{M \times 1}\|_2^2 + \gamma \|\boldsymbol{\sigma}_{M \times 1}\|_1 \right\} \tag{4}
$$

is used to accomplish the azimuth processing and reconstruct the image in this study. Here, $\|\cdot\|_1$ and $\|\cdot\|_2$ represent l_1-norm and l_2-norm, respectively [20]. γ is a trade-off parameter balancing sparsity and the quality of fitness.

Usually, the noise $\mathbf{n}_{N \times 1}$ is assumed to satisfy Gaussian distribution with zero-mean and variance σ_n^2 [19]. Under this assumption, maximum a posteriori (MAP) estimation explains that the approximation equation in (4) equals adopting the Laplace prior on the vector $\boldsymbol{\sigma}_{M \times 1}$ [19], [21]. Simultaneously, Laplace priors heavily enforce the sparsity constraint so that most elements of $\boldsymbol{\sigma}_{M \times 1}$ close to zero are preferred. However, using the Laplace prior directly to analyse various prior on the vector $\boldsymbol{\sigma}_{M \times 1}$ is not readily accomplished. Different priors corresponding to different hypotheses about underlying truth can be invoked [22]. The prior distribution of a scene backscattering cross-section is affected by the observation incidence angle, wavelength, and surface structure, and many effect factors are not totally accounted for

by a simple deterministic model [23]. Therefore, we hope to achieve the prior distribution from an SAR image, although speckle noise exists. The statistics of SAR images have been investigated under the assumption of Gaussian statistics for the backscattering cross-section [24], [25]. The simulation in Fig. 2 takes ships on the ocean as an example of a sparse scene to analyze in this study, and it also validates that the backscattering cross-section of ships on the ocean obeys the Gaussian distribution.
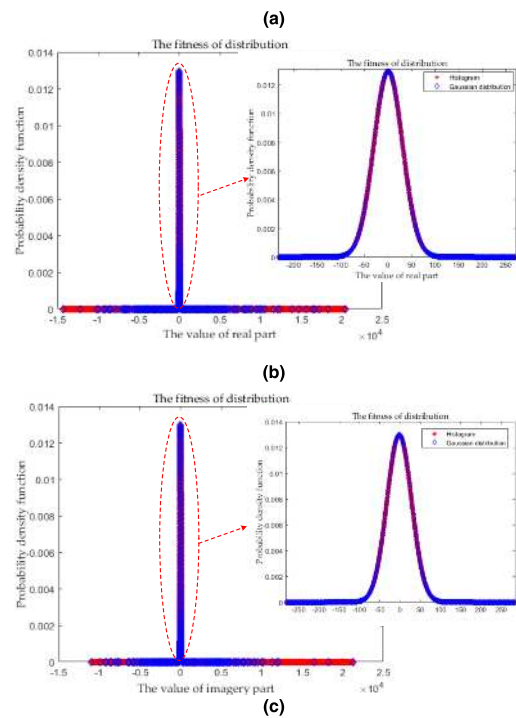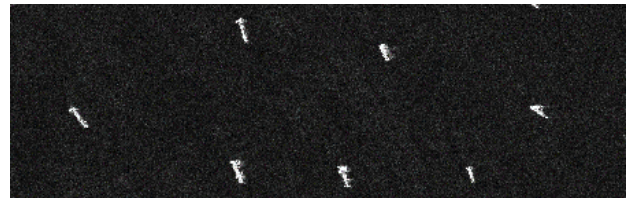

FIGURE 2. (a) is an SAR image of ships on the ocean. (b) and (c) are the statistical distributions of the real and imaginary parts of the SAR image in (a), respectively. The histogram of SAR image data fits well with a Gaussian distribution with a nearly zero mean.

Therefore, this kind of sparse scene satisfies the Gaussian distribution with zero-mean and variance σ_x^2. Under the above assumption about the noise $\mathbf{n}$ without the subscript, it means the following:

$$
\begin{cases} p_{\mathbf{n}}(\mathbf{n}) = p_{\mathbf{s}|\boldsymbol{\sigma}}(\mathbf{s}|\boldsymbol{\sigma}) = \frac{1}{\sqrt{2\pi}\sigma_n} \exp\left\{ -\frac{\|\mathbf{s} - \mathbf{D}\boldsymbol{\sigma}\|_2^2}{2\sigma_n^2} \right\} \\ p_{\boldsymbol{\sigma}}(\boldsymbol{\sigma}) = \frac{1}{\sqrt{2\pi}\sigma_x} \exp\left\{ -\frac{\|\boldsymbol{\sigma}\|_2^2}{2\sigma_x^2} \right\}, \end{cases} \tag{5}
$$

The reconstruction performance based on CS is interesting. As the reconstructed algorithm is an estimation method,

a classical point target evaluation system (e.g., 3 dB resolution, PSLR and ISLR) is not available in the CS-SAR system. For a given vector $\boldsymbol{\sigma}$, the reconstruction performance can be evaluated using the estimation error $E\{\hat{\boldsymbol{\sigma}} - \boldsymbol{\sigma}\}^2\}$, where $\hat{\boldsymbol{\sigma}}$ is the reconstruction result, and $\boldsymbol{\sigma}$ is the real backscattering cross-section. Under the distribution in (5), the reconstruction performance of $\hat{\boldsymbol{\sigma}}$ satisfies (see APPENDIX I)

$$
\begin{aligned}
E &\left\{ (\hat{\boldsymbol{\sigma}} - \boldsymbol{\sigma})^2 \right\} \\
&\geq \left\{ -E\left[\frac{\partial^2 \ln p_{s/\sigma}\,(s/\sigma)}{\partial \sigma^2} \right] - E\left[\frac{\partial^2 \ln p_{\sigma}\,(\sigma)}{\partial \sigma^2} \right] \right\}^{-1} \\
&\geq o\,(\log(M)) \cdot trace\left[\left(\frac{\mathbf{F}_{N\times S}^H \mathbf{F}_{N\times S}}{\sigma_n^2} + \frac{\mathbf{I}}{\sigma_x^2} \right)^{-1} \right] \\
&> \frac{o(\log(M)) \cdot S \cdot \sigma_x^2}{SNR \cdot L \cdot \left[1 + 1/2 \cdot (1-u) \right] + 1}, \quad (6)
\end{aligned}
$$

where $trace\,(\cdot)$ denotes the trace of a matrix, and $SNR = \sigma_x^2/\sigma_n^2$ is the signal-to-noise ratio in the SAR image. $\mathbf{I}$ is the unit matrix. L is the number of samples in one aperture time and is proportional to the number of samples N when the scene size M is certain. The mutual coherence coefficient as follows:

$$
u = \max_{1 \leq m_1 \neq m_2 \leq M} \frac{\left| \langle \mathbf{D}_{m_1}, \mathbf{D}_{m_2} \rangle \right|}{\left\| \mathbf{D}_{m_1} \right\|_2 \cdot \left\| \mathbf{D}_{m_2} \right\|_2} \quad (7)
$$

reflects the maximum similarity between any two different columns m_1, m_2 in $\mathbf{D}_{N\times M}$. $\mathbf{F}_{N\times S}$ is the submatrix formed by taking S columns from $\mathbf{D}_{N\times M}$, which are specified by the index vector $\boldsymbol{\Lambda}$ and each element in $\boldsymbol{\Lambda}$ satisfies the following:

$$
\sigma_{\Lambda_l} \gg 0 \quad (l = 1, 2, \cdots, S).
$$

The inequality (6) indicates that a higher number of samples N, larger SNR and smaller u lead to better reconstruction performance. This study uses sub-Nyquist sampling for every sub-swath, which reduces the number of samples N and affects the mutual coherence coefficient u. To compensate for the deterioration of reconstruction performance owing to the decrease of N, SNR can be improved by increasing the transmitting power. The error caused by u can only be compensated for by choosing the optimum sub-Nyquist sampling principle to make u as small as possible, which is discussed in the next section.

III. PSEUDO-RANDOM SUB-NYQUIST SAMPLING

Restricted isometry property (RIP) of the reconstructed matrix $\mathbf{D}_{N\times M}$ is a sufficient and necessary condition for reconstructing a sparse scene [26]. RIP implies that randomness plays a crucial role in constructing the reconstructed matrix. The more random the reconstructed matrix is, the more easily RIP is satisfied. The sub-Nyquist sampling method and the form of the azimuth receiving signals affect the randomness of the reconstructed matrix. The azimuth receiving signal in an SAR system is decided by the Doppler movement between movement platform and the

observed scene, and it does not have randomness. Therefore, the randomness of the reconstructed matrix is improved by the sub-Nyquist sampling method.

Random sub-Nyquist sampling is a commonly used method for reconstructing sparse signals, and achieves good performance [27]. Fig. 3(a) demonstrates the corresponding azimuth sampling series. From the perspective of probability theory, each sampling instant η in random sub-Nyquist sampling method is a continuous random variable with probability density $p\,(\eta)$ in the $[0, T_1]$ interval. All the sampling instants are mutually independent and identically distributed, and mean value $\bar{u}_r$, the numerical characteristic of random variable, is used to substitute the mutual coherence u_r in random sub-Nyquist sampling method (see APPENDIX II) as follows:

$$
\begin{aligned}
\bar{u}_r = \lim_{A\to\infty} &\sum_{i_{n_f}=0}^{A} \sum_{i_{(n_f+1)}=0}^{A} \cdots \\
&\sum_{i_{n_l}=0}^{A} \left(\left| \sum_{n=n_f}^{n_l} \exp\left\{ j \frac{4\pi V_e d}{\lambda R_0} \left(\frac{i_n}{A} T_1 \right) \right\} \right| \cdot \left(\frac{i_{n_f}}{A} T_1 \right) \right. \\
&\left. \cdot p\left(\frac{i_{n_f+1}}{A} T_1 \right) \cdots p\left(\frac{i_{n_l}}{A} T_1 \right) \cdot \frac{T_1}{A} \cdot \frac{T_1}{A} \cdots \frac{T_1}{A} \right) \Big/ L^2, \\
&\hspace{10cm} (8)
\end{aligned}
$$

where n_f and n_l are the first and last index of a row in which elements of two columns with maximum correlation are non-zero, respectively. V_e is the equivalent velocity of the satellite. R_0 is the nearest slant range between SAR and the M point targets. d is the ground spacing between two point targets corresponding to two columns with maximum
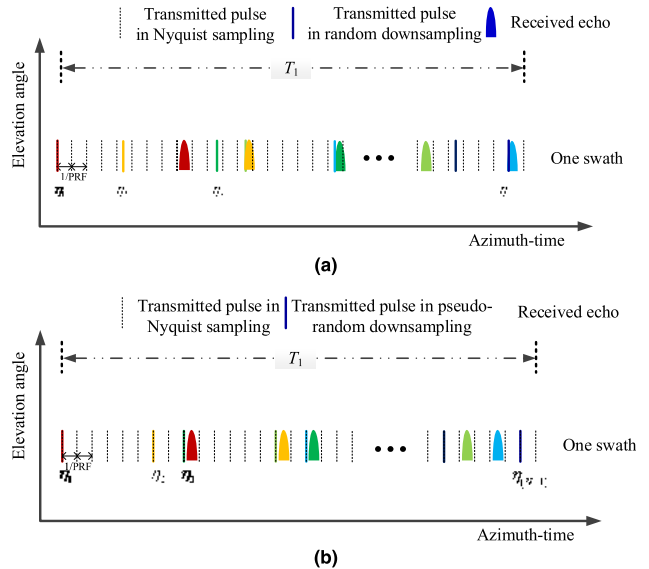

FIGURE 3. Comparison between the random and pseudo-random down-sampling. (a) shows the conflict between the transmitting pulses and echoes caused by the random sampling. (b) illustrates that only one pulse is randomly selected from Q consecutive Nyquist pulses with a certain PRF, which avoids the conflict in (a).

correlation. L denotes the l_2-norm of one column. The random sub-Nyquist sampling can achieve small u, because it can break the correlation inside the azimuth signal. However, random sub-Nyquist sampling method possibly causes the conflict between the transmitting and the receiving because SAR system uses a common antenna to transmit pulse signals and receive echoes, as shown in Fig. 3(a). Considering this unavoidably conflict, a pseudo-random sub-Nyquist sampling is proposed. As shown in Fig. 3(b), samples in pseudo-random sub-Nyquist sampling method are randomly chosen from the number of Nyquist samples N_{Nyquist} with a certain PRF. Each sampling instant η in this sub-Nyquist sampling method is a discrete random variable and the set of possible values is as follows:

$$\Omega = \left\{ \frac{T_1}{N_{\text{Nyquist}} - 1} \cdot 0, \frac{T_1}{N_{\text{Nyquist}} - 1} \cdot 1, \cdots, \right.$$
$$\left. \frac{T_1}{N_{\text{Nyquist}} - 1} \cdot (N_{\text{Nyquist}} - 1) \right\}, \quad (9)$$

where N_{Nyquist} is the number of Nyquist samples with a certain PRF. Similarly, mean value u_{pr}, i.e., the numerical characteristic of a random variable, is used to substitute the mutual coherence u_{pr} in the pseudo-random sub-Nyquist sampling method as follows: (see APPENDIX II)

$$\bar{u}_{pr} = \sum_{i_{n_f}=0}^{N_{\text{Nyquist}}-1} \sum_{i_{(n_f+1)}=0}^{N_{\text{Nyquist}}-1} \cdots \sum_{i_{n_l}=0}^{N_{\text{Nyquist}}-1}$$
$$\times \left(\left| \sum_{n=n_f}^{n_l} \exp\left\{ j\frac{4\pi V_e d}{\lambda R_0} \cdot \left(\frac{i_n}{N_{\text{Nyquist}} - 1} T_1 \right) \right\} \right| \right.$$
$$\cdot p\left(\frac{i_{n_f}}{N_{\text{Nyquist}} - 1} \cdot T_1 \right) \cdot p\left(\frac{i_{(n_f+1)}}{N_{\text{Nyquist}} - 1} \cdot T_1 \right)$$
$$\cdots p\left(\frac{i_{n_l}}{N_{\text{Nyquist}} - 1} \cdot T_1 \right)$$
$$\left. \cdot \frac{T_1}{N_{\text{Nyquist}}} \cdot \frac{T_1}{N_{\text{Nyquist}}} \cdots \frac{T_1}{N_{\text{Nyquist}}} \right) \Big/ L^2, \quad (10)$$

Equation (8) and Equation (10) denote the summation of the infinite and finite series, respectively. When the number of finite series N_{Nyquist} is very large and the interval length T_1 is very small, the summation of the infinite series is nearly equal to the summation of the finite series. In SAR system, the number of Nyquist samples N_{Nyquist} is very large and the sampling duration T_1 is very small, so $u_r \approx u_{pr}$. The simulation shown in Fig. 4 also verifies this, and the corresponding simulation parameters are given in Table 1. Therefore, pseudo-random down-sampling can achieve optimal performance and is adopted in this study.

IV. SPACE-TIME SAMPLING AND AGILESAR

Based on pseudo-random sub-Nyquist sampling, a novel time–space sampling is proposed to achieve wide swath for the sparse scene in a spaceborne SAR system, illustrated in Fig. 5. Like the existing wide-swath working modes, e.g.,
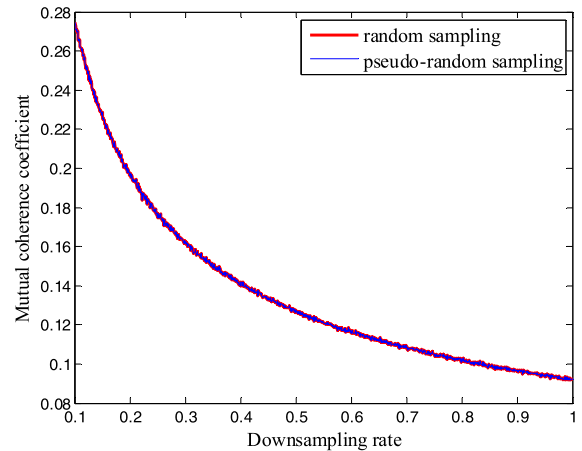

FIGURE 4. Illustration of mutual coherence coefficients. Two curves approximately overlap, which indicates that the mutual coherence coefficients achieved by random and pseudo-random sub-Nyquist sampling are basically the same.

TABLE 1. Simulation parameters.

Parameters	Values	Range of parameters
Orbital height (km)	693	Low earth orbit height [28]
Wavelength (m)	0.0555	0.025~1.3 [1]
Incidence angles (°)	38.73~43.50	15~70
Mean time interval of transmitting pulse under random sampling (µs)	0.0025	<0.0032
Mean time interval of transmitting pulse under pseudo-random sampling (µs)	0.0025	<0.0032

ScanSAR [29] and TOPSAR [30], wide-swath coverage is also mosaicked by several range sub-swaths. 'Time sampling' of time–space sampling means the pseudo-random sub-Nyquist sampling on the azimuth dimension, and 'space sampling' of time–space sampling means the range beam is adjusted to observe different sub-swaths generally after one or two pulse intervals. During the observation period, the SAR system transmits pulses at the rate of PRF and receives echoes. Suppose there are Q sub-swaths. $\lfloor N_{\text{Nyquist}}/Q \rfloor$ pulses from N_{Nyquist} consecutive Nyquist pulses with a certain PRF are randomly selected for one sub-swath, which indicates that the sampling method for every sub-swath satisfies the pseudo-random sub-Nyquist sampling principle presented in Section III, where $\lfloor \bullet \rfloor$ is the floor function. N_{Nyquist} consecutive Nyquist pulses with a certain PRF are allocated to Q sub-swaths.

We name this working mode AgileSAR in this study because the beam must be adjusted towards different sub-swaths between adjacent pulses if two adjacent pulses are not assigned to the same sub-swath.

A. AGILESAR

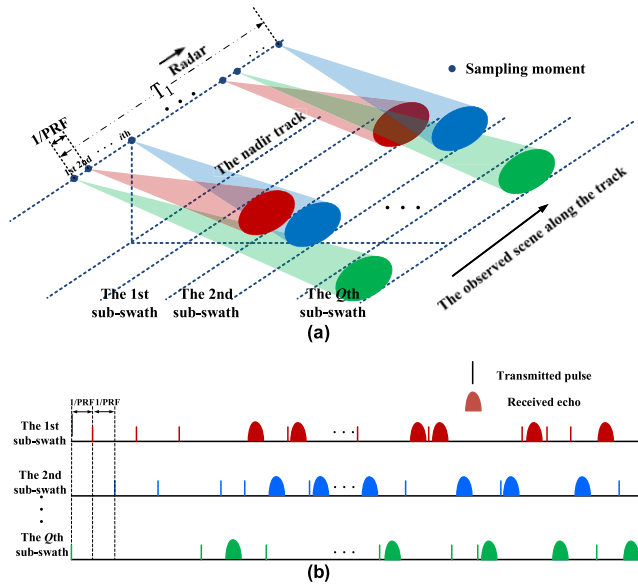To introduce AgileSAR, it is compared with TOPSAR:

FIGURE 5. Illustration of AgileSAR. (a) shows the geometry between SAR and the swath. Different sub-swaths correspond to different squint angles. The maximum squint angle is applied to the first sub-swath. The Qth sub-swath is observed with zero squint angle. (b) demonstrates the relationships between transmitting pulses and echoes. Although the AgileSAR works at the rate of PRF, the average sampling rate for every sub-swath is only 1/Q of PRF.

1) TIME INTERVAL OF SAMPLES IN EACH SUB-SWATH

Transmitting one pulse is essentially one sample in SAR system. From the perspective of trans-receiver, the time interval of every two pulses is certain and satisfies the Nyquist sampling theorem. However, from the perspective of the sampled sub-swath, the time interval of every two samples in each sub-swath is not certain and the average sampling frequency is smaller than the Nyquist frequency in AgileSAR. In comparison, PRF satisfies the Nyquist sampling theorem in each sub-swath of TOPSAR to guarantee an exact reconstruction of scene. The antenna beam steers to the different sub-swath after TOPSAR transmits many pulses during the dwell time, which is designed to meet azimuth resolution, but the beam steers to a different sub-swath after one or two pulses in AgileSAR.

2) JUMPING RULE OF THE RANGE ANTENNA BEAM AMONG ALL THE SUB-SWATHS

After the dwell time, the antenna beam of TOPSAR jumps from the qth sub-swath to the $(q + 1)$th sub-swath or from the Qth sub-swath to 1st sub-swath, where $q \in \{1, 2, \cdots, (Q - 1)\}$ is the serial number of the sub-swath. In AgileSAR, the antenna beam randomly jumps to any one of all the sub-swaths to transmit one pulse after receiving one echo, and then the antenna beam leaps on the sub-swath of echo arrival to receive the echo.

3) ROTATING RULE OF AZIMUTH ANTENNA

In TOPSAR, the azimuth antenna has a dwell time in each sub-swath and rotates the antenna throughout the dwell time

from backward to forward. The rotating angle of antenna continuously varies. This rotating mechanism guarantees the consistency of antenna weighting and the azimuth ambiguity in each sub-swath to solve the problems of scalloping and azimuth-varying ambiguities. In AgileSAR, to avoid the overlap among the echoes of different sub-swaths as the swath is ultra-wide and the conflict between transmitting and receiving as illustrated in Fig. 3(a), it adopts squinted acquisition to make the echo delays of all the sub-swaths same. Except the sub-swath with the biggest incidence angle working in the side-looking scheme, all the sub-swaths have specific squint angles, the squint angle of each sub-swath is as follows:

$$\theta_q = \arccos\left(R_q/R_Q\right),$$
$$0 \leq \theta_q \leq \pi/2, \quad q = 1, 2, \cdots, (Q - 1), \quad (11)$$

where q is the serial number of the sub-swath from small incidence to large incidence. θ_q denotes the squint angle of the qth sub-swath. R_q is the slant range on the center beam of the qth sub-swath. R_Q is the slant range on the center beam of the Qth sub-swath. (11) indicates that the closer the sub-swath away from the nadir is, the larger the squint angle is.

When the range antenna beam jumps from one sub-swath to another sub-swath, accordingly the azimuth antenna also rotates from one squint angle to another squint angle. The rotating angle of antenna discretely and randomly varies, and only has Q values. After the squinting scheme, all the sub-swaths have the same echo delays, and the PRF of transmitting pulses is certain. Therefore, like the transmitting and receiving method in one sub-swath in TOPSAR, AgileSAR also adopts the same method, i.e., it transmits one pulse and then receives one echo from the perspective of the trans-receiver.

4) AZIMUTHAL SPECTRUM WIDTH

In the TOPSAR mode, the antenna beam dwells on one sub-swath for a period of time determined by the azimuth resolution and jumps to the next sub-swath. As a result, the corresponding azimuthal spectrum width for each sub-swath is approximately $1/(Q + 1)$ of the entire Doppler bandwidth decided by the azimuth antenna length, which results in decreased azimuth resolution. Although the azimuthal spectrum corresponding to each sub-swath is sparse for AgileSAR, its span is equal to the entire Doppler bandwidth. This lays a good foundation for the image reconstruction with full resolution based on CS.

5) DATA PROCESSING ALGORITHM

For the transmitting signals in these two working modes, both of which are linear frequency modulated (LFM) signals, the range compression methods are the same. Range migration of TOPSAR data is corrected using the $\sin c$ function interpolation method or frequency scaling method [2] while AgileSAR corrects range migration by back projection [31]. Here, matched filtering (MF) or CS can be adopted to compress the azimuth signals satisfying the Nyquist theorem in

TOPSAR, and the azimuth signals in AgileSAR are compressed only based on CS. The details of the processing algorithm are explained later.

B. ALGORITHM OF RECONSTRUCTION

Section II already mentioned that no matter which algorithm is adopted, the algorithm of reconstruction includes three steps: the range compression, RCMC, and the azimuth compression. The demonstration of the reconstruction process is as follows:

1) RANGE COMPRESSION

As long as the transmitted signal is an LFM signal, the range signal can be compressed based on MF [2]. Assuming that matched filter $H(f_\tau)$ of the range signal in the frequency domain is denoted as follows:

$$H(f_\tau) = rect\left(\frac{f_\tau}{|K_r|T_r}\right)\exp\left(j\pi\frac{f_\tau^2}{K_r}\right), \quad (12)$$

the signal $s_{rc}(\tau, \eta)$ after range compression is achieved by the following:

$$
\begin{aligned}
s_{rc}(\tau, \eta) \\
&= \text{IFFT}_\tau\{S_0(f_\tau, \eta)H(f_\tau)\} \\
&= \sum_{m=1}^{M}\sigma_m W_m(\tau, \eta)T_r \cdot \sin c\left\{K_r T_r\left[\tau - \frac{2R_m(\eta_{c_m})}{c}\right]\right\} \\
&\quad \cdot \exp\left\{-\frac{j4\pi R_m(\eta)}{\lambda}\right\} + n(\tau, \eta).
\end{aligned}
\quad (13)
$$

where $S_0(f_\tau, \eta)$ is the Fourier transform of the signal $s_0(\tau, \eta)$ in the range and $\text{IFFT}_\tau\{\cdot\}$ is the inverse Fourier transform in the range.

2) RCMC

In the traditional SAR system, the azimuthal signal is nearly an LFM signal so that there is one-to-one and linear correspondence between the time domain and frequency domain in the azimuth dimension. Because targets in the same range cell have the same range migration in the azimuth frequency domain, most algorithms, e.g., range Doppler algorithm [2] and chirp scaling algorithm [2], correct range cell migration in the azimuth frequency domain. To correct the range migration of one target is equivalent to correcting that of all the targets in the same range cell, so that correcting range migration in the azimuth frequency domain is highly efficient. In the AgileSAR system, sampling is non-uniform so that the frequency also non-uniformly varies and the range migrations of the targets on the same range cell are different in the azimuth frequency domain. RCMC is implemented in the azimuth time domain in this study. The procedure of RCMC is: i) First, it should choose the imaging area that is guaranteed to contain all targets in the raw data. For the cell division of the imaging area, even if the cell of the imaging area is divided more precisely, the resolution will not change, which seriously affects the imaging efficiency. Therefore, the cell

TABLE 2. AgileSAR parameters.

Parameters	Values	Range of parameters
Orbital height (km)	693	Low earth orbit height [28]
Wavelength (m)	0.0555	0.025~1.3 [1]
Signal bandwidth (MHz)	100	100
Antenna height (m)	8.93	8.93
Antenna length (m)	3.793	3.793
Average power (W)	1413	1413

division of the imaging area should be slightly smaller than or equal to that in the raw data. ii) It takes the ascending sampling to range dimension of raw data. To calculate the slant range from each division cell of imaging area to radar at each sampling instant, find the position of each division cell at each azimuth sampling instant on the ascending sampling range cell and take the data on this position. Sum up the data of division cell on the same nearest slant range. After RCMC, the signal is denoted as (2).

3) AZIMUTH COMPRESSION

Based on the analysis in section II, the azimuth signal in sub-Nyquist sampling method can be recovered by the optimization equation (4) in AgileSAR system.

C. ANALYSIS OF RECONSTRUCTED PERFORMANCE

In addition to the swath width and spatial resolution, the reconstruction performance should be compared with conventional SAR. As mentioned in Section II, CS is applied to reconstruct sparse signals. Here, the least square (LS) is adopted to process the signals satisfying the Nyquist theorem, and the estimation $\widehat{\sigma}_{LS}$ satisfies the following:

$$E\left\{(\widehat{\sigma}_{LS} - \sigma)^2\right\} > \frac{o(\log(M)) \cdot S \cdot \sigma_x^2}{SNR \cdot L \cdot \left[1 + 1/2 \cdot (1 - \bar{u}_{pr}) \cdot u_{LS}/\bar{u}_{pr}\right]}. \quad (14)$$

where $\bar{u}_{pr}$ and u_{LS} are the mean mutual coherence in (10) and the mutual coherence in (7).

By comparing (6) and (14), it can be observed that the factors influencing the estimation error are the mutual coherence coefficient, the number of samples, and *SNR*. AgileSAR uses pseudo-random sub-Nyquist sampling to make $\bar{u}_{pr}$ approach u_{LS}, and improves *SNR* by increasing the transmitting power to make the multiplication of *SNR* and *L* a constant. As a result, the lower bounds of the l_1 approximation method and LS estimation are almost equal, and the reconstruction performances for AgileSAR and the conventional SAR are approximately the same.

V. VALIDATION AND ANALYSIS

After having understood the observation method of Agile-SAR, a design example is presented so that the reader can comprehend the expected wide swath system. The system parameters decide the performance of the SAR system. Some system parameters are typical of a conventional SAR system,

TABLE 3. Parameters and specifications for every sub-swath.

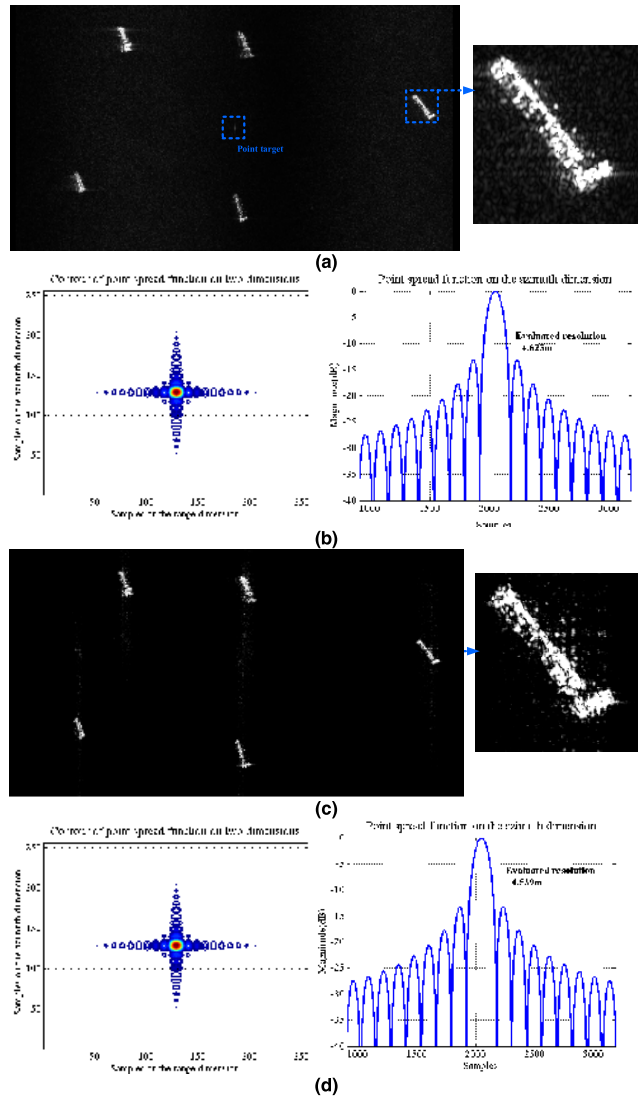| Parameters	S1	S2	S3	S4	S5
Incidence angles (°)	23.54~27.84	26.87~31.18	30.47~34.86	34.47~38.97	38.73~43.50
Squint angles (°)	31.07	28.37	24.56	18.40	0
Sub-swath (km)	56	59	64	71	83

(a)

(b)

(c)

(d)

FIGURE 6. Reconstruction results. The ships enclosed by the red rectangles are enlarged to be the right parts. Compared with the result achieved by the conventional SAR, i.e., (a), the main details of ships are preserved in (c), i.e., the result corresponding to the AgileSAR. Although the sampling is sparse in AgileSAR, satisfactory reconstruction performance is achieved. A single point target is placed in the middle of the scene to evaluate the resolution, and the corresponding point spread functions on two dimensions and on the azimuth dimension are illustrated in (b) and (d), respectively.

such as the incidence angle and squint angle of the sub-swath. Other parameters, i.e., the selected time–space sampling method and the estimation error, are peculiar to AgileSAR. These are described in sections III and IV, respectively. Compared with Sentinel-1, which can acquire 5-m resolution and

TABLE 4. Simulation parameters for conventional SAR.

Parameters	Values	Range of parameters
Orbital height (km)	693	Low earth orbit height [28]
Wavelength (m)	0.0555	0.025~1.3 [1]
Signal bandwidth (MHz)	100	100
Incidence angles (°)	38.73~43.50	Incidence angles in Table III
Squint angles (°)	0	Squint angles in Table III
PRF(Hz)	1947	1947

80-km swath in the strip mapping mode [32], AgileSAR can realize the same resolution and a wide swath of 300 km using a single azimuth-channel, for which the design parameters are listed in Table 2. To cover the 300-km swath, the swath is composed of five sub-swaths. The spaceborne AgileSAR transmits one pulse every 513.6 μs. For every sub-swath, the average PRF is 389.4 Hz. In addition to resolution and the swath width, the incidence and squint angles corresponding to every sub-swath are also listed in Table 3.

Although the sampling is sparse, the span of the Doppler frequency shift for targets in every sub-swath is unchanged so that the resolution is preserved. Therefore, the achieved azimuth resolutions are the same as those of a conventional SAR system while a wide continuous swath is covered. To demonstrate the reconstruction performance, simulations of AgileSAR and the conventional SAR are compared. One TerraSAR-X image is selected and put at the 5th sub-swath in the AgileSAR simulation. The corresponding result is shown in Fig. 6(c). For conventional SAR simulation, the parameters are given in Table 4, and the result is shown in Fig. 6(a). By comparing Fig. 6(a) and (c), the main details of the target remain, which indicates that the reconstruction performance of AgileSAR approaches that of conventional SAR. A single point target is placed in the middle of the scene to evaluate the resolution, and the evaluated resolution in Fig. 6(d) is approximately the same as in (b).

VI. CONCLUSION

This paper presents a novel time-space sampling method for spaceborne SAR to increase the swath width while preserving the resolution. Moreover, the following two major findings have been obtained:

(1) From the deducted mean square error, we analyse that a higher number of samples N, larger SNR and smaller u lead to better reconstruction performance when the scene size M is certain. The pseudo-random sub-Nyquist sampling method is analysed and has nearly the same mutual coherence as random sub-Nyquist sampling, so that it can achieve optimal reconstruction performance and avoid the conflict between the transmitting and receiving on one sub-swath when the number of samples and SNR are certain.

(2) When the pseudo-random sub-Nyquist sampling method is applied on Q sub-swaths, the overlap between transmitting and receiving still exists. This study adopts the

squinting scheme to let all sub-swathes have the same echo delays. Simultaneously, to guarantee the reconstruction quality of SAR images compared with the conventional method, it should increase transmitting power.

The observed mode is applied to not only the strip mapping mode but also other modes such as sliding spotlight and TOPS modes. Further research will focus on developing the source of generating random waveforms in the SAR system, when the first category of sub-Nyquist sampling method is analyzed and applied.

APPENDIX I

The equation (3) without subscript is rewritten as follows:

$$\mathbf{s} = \mathbf{D}\boldsymbol{\sigma} + \mathbf{n}. \tag{15}$$

A. PROOF OF FORMULA (6)

Assuming that the vector $\boldsymbol{\sigma}$ is a random variable vector, the mean square error (MSE) of the estimation $\hat{\boldsymbol{\sigma}}$ in a Bayesian framework is denoted by [34] the following:

$$\mathrm{MSE}\left(\hat{\boldsymbol{\sigma}}\right)$$

$$= \sum_{m=1}^{M} E\left\{\left(\hat{\sigma}_m - \sigma_m\right)^2\right\}$$

$$\geq trace\left(\left\{-E\left[\frac{\partial^2 \ln p_{\mathbf{s},\sigma}\left(\mathbf{s},\boldsymbol{\sigma}\right)}{\partial\sigma_{m1}\partial\sigma_{m2}}\right]\right\}^{-1}\right)$$

$$= trace\left(\left\{-E\left[\frac{\partial^2 \ln p_{\mathbf{s}/\sigma}\left(\mathbf{s}/\boldsymbol{\sigma}\right)}{\partial\sigma_{m1}\partial\sigma_{m2}}\right] - E\left[\frac{\partial^2 \ln p_\sigma\left(\boldsymbol{\sigma}\right)}{\partial\sigma_{m1}\partial\sigma_{m2}}\right]\right\}^{-1}\right). \tag{16}$$

where $\hat{\sigma}_m$ and σ_m are the mth elements of $\hat{\boldsymbol{\sigma}}$ and $\boldsymbol{\sigma}$, respectively. $trace\left(\cdot\right)$ denotes the trace of a matrix. $p_{\mathbf{s},\sigma}\left(\mathbf{s},\boldsymbol{\sigma}\right)$, $p_{\mathbf{s}/\sigma}\left(\mathbf{s}/\boldsymbol{\sigma}\right)$ and $p_\sigma\left(\boldsymbol{\sigma}\right)$ are the joint probability density function of the vector $\mathbf{s}$ and $\boldsymbol{\sigma}$, the conditional probability density function of the vector $\mathbf{s}$ and $\boldsymbol{\sigma}$, and the prior probability density function of the vector $\boldsymbol{\sigma}$, respectively. The data information matrix $\mathbf{J}_\mathrm{D}$ and the prior information matrix $\mathbf{J}_\mathrm{P}$ represent

$$-E\left[\frac{\partial^2 \ln p_{\mathbf{s}/\sigma}\left(\mathbf{s}/\boldsymbol{\sigma}\right)}{\partial\sigma_{m1}\partial\sigma_{m2}}\right] \text{ and } -E\left[\frac{\partial^2 \ln p_\sigma\left(\boldsymbol{\sigma}\right)}{\partial\sigma_{m1}\partial\sigma_{m2}}\right],$$

respectively.

The following analyses the Bayesian information matrix $\mathbf{J}_\mathrm{B} = \mathbf{J}_\mathrm{D} + \mathbf{J}_\mathrm{P}$ from these two information matrices:

1) Calculation of the data information matrices $\mathbf{J}_\mathrm{D}$:

$$\mathbf{J}_\mathrm{D} = -E\left[\frac{\partial^2 \ln p_{\mathbf{s}/\sigma}\left(\mathbf{s}/\boldsymbol{\sigma}\right)}{\partial\sigma_{m1}\partial\sigma_{m2}}\right]$$

$$= E\left[\frac{1}{2\sigma_n^2} \cdot \frac{\partial \|\mathbf{s} - \mathbf{D}\sigma\|_2^2}{\partial\sigma_{m1}\partial\sigma_{m2}}\right]$$

$$= E\left\{\frac{1}{2\sigma_n^2} \cdot \frac{\partial}{\partial\sigma_{m1}\partial\sigma_{m2}}\left[\mathbf{s}^H\mathbf{s} - \mathbf{s}^H\mathbf{D}\sigma\right.\right.$$

$$\left.\left. -\sigma^H\mathbf{D}^H\sigma + \sigma^H\mathbf{D}^H\mathbf{D}\sigma\right]\right\}$$

$$= E\left\{\frac{1}{2\sigma_n^2} \cdot \frac{\partial}{\partial\sigma_{m2}}\left[2\mathbf{D}^H\mathbf{D}\sigma - 2\mathbf{D}^H\mathbf{s}\right]\right\}$$

$$= \frac{\mathbf{D}^H\mathbf{D}}{\sigma_n^2} \tag{17}$$

2) Calculation of the prior information matrix $\mathbf{J}_\mathrm{P}$ as follows:

$$\mathbf{J}_\mathrm{P} = -E\left[\frac{\partial^2 \ln p_\sigma\left(\boldsymbol{\sigma}\right)}{\partial\sigma_{m1}\partial\sigma_{m2}}\right] = E\left[\frac{1}{2\sigma_x^2} \cdot \frac{\partial \|\boldsymbol{\sigma}\|_2^2}{\partial\sigma_{m1}\partial\sigma_{m2}}\right]$$

$$= \frac{\mathbf{I}}{\sigma_x^2}, \tag{18}$$

where $\mathbf{I}$ is the unit matrix. Substituting (17) and (18) into (16), we obtain the following:

$$E\left\{\left(\hat{\boldsymbol{\sigma}} - \boldsymbol{\sigma}\right)^2\right\} \geq \left(\frac{\mathbf{D}^H\mathbf{D}}{\sigma_n^2} + \frac{\mathbf{I}}{\sigma_x^2}\right)^{-1}$$

$$\geq trace\left[\left(\frac{\mathbf{D}^H\mathbf{D}}{\sigma_n^2} + \frac{\mathbf{I}}{\sigma_x^2}\right)^{-1}\right]. \tag{19}$$

References [34] and [35] explains that the estimation error is a logarithmic factor of the oracle performance as follows:

$$E\left\{\left(\hat{\boldsymbol{\sigma}} - \boldsymbol{\sigma}\right)\right\} \geq o\left(\log M\right) \cdot trace\left[\left(\frac{\mathbf{F}^H\mathbf{F}}{\sigma_n^2} + \frac{\mathbf{I}}{\sigma_x^2}\right)^{-1}\right]. \tag{20}$$

Assume that $\mathbf{A} = \mathbf{F}^H\mathbf{F}$, $\mathbf{B} = \left(\frac{\mathbf{F}^H\mathbf{F}}{\sigma_n^2} + \frac{\mathbf{I}}{\sigma_x^2}\right)$, and their eigenvalues are $\lambda_1, \lambda_2, \cdots, \lambda_S$ and $\alpha_1, \alpha_2, \cdots, \alpha_S$, respectively. Based on the structure form of the reconstructed matrix $\mathbf{D}_{N\times M}$ in (3) during the reconstruction, the element of the reconstruction matrix ignores the weighting, and l_2-norm of each column are nearly equal and assuming $\|\mathbf{D}_l\|_2^2 \approx L$, where L is the number of samples in one aperture time. L is proportional to the number of samples N when the point target M is certain. Then, $\sum_{l=1}^{S}\lambda_l = L \cdot S, \alpha_l = \frac{1}{\sigma_x^2}\left(SNR \cdot \lambda_l + 1\right)$ and

$$\sum_{l=1}^{S}\lambda_l \cdot \sum_{l=1}^{S}\lambda_l^{-1} \geq S^2 \Rightarrow \sum_{l=1}^{S}\lambda_l^{-1} \geq \frac{S}{L}$$

$$\sum_{l=1}^{S}\alpha_l \cdot \sum_{l=1}^{S}\alpha_l^{-1} \geq S^2 \Rightarrow \sum_{l=1}^{S}\alpha_l^{-1} \geq \frac{S^2 \cdot \sigma_x^2}{\sum_{l=1}^{S}\left(SNR \cdot \lambda_l + 1\right)}$$

$$= \frac{S \cdot \sigma_x^2}{SNR \cdot L + 1}$$

Gail's circle theorem indicates that

$$\left|\alpha_l - \frac{SNR \cdot L + 1}{\sigma_x^2}\right| \leq \bar{u}_{pr}\left(S - 1\right) \cdot \frac{SNR \cdot L}{\sigma_x^2}$$

$$\frac{SNR \cdot L + 1}{\sigma_x^2} - \bar{u}_{pr}\left(S - 1\right) \cdot \frac{SNR \cdot L}{\sigma_x^2}$$

$$\leq \alpha_l \leq \frac{SNR \cdot L + 1}{\sigma_x^2} + \bar{u}_{pr}\left(S - 1\right)$$

$$\cdot \frac{SNR \cdot L}{\sigma_x^2}$$

Therefore,

$$\sum_{l=1}^{S} \alpha_l^{-1} \geq \frac{S \cdot \sigma_x^2}{SNR \cdot L \cdot \left[1 + \bar{u}_{pr}\left(S - 1\right)\right] + 1}$$

$$E\left\{(\widehat{\sigma} - \sigma)^2\right\} \geq \frac{o(\log M) \cdot S \cdot \sigma_x^2}{SNR \cdot L \cdot \left[1 + \bar{u}_{pr}\left(S - 1\right)\right] + 1}$$

Reference [36] indicates that the sharpness bound is $S < \frac{1}{2}\left(\frac{1}{\bar{u}_{pr}} + 1\right)$, so

$$E\left\{(\widehat{\sigma} - \sigma)^2\right\} \geq \frac{o(\log(M)) \cdot S \cdot \sigma_x^2}{SNR \cdot L \cdot \left[1 + 1/2 \cdot (1 - \bar{u}_{pr})\right] + 2} \quad (21)$$

B. PROOF OF FORMULA (14)

When LS is adopted to process the signals, the estimation error is [30] as follows:

$$MSE\left(\widehat{\sigma}\right) = \sigma_n^2 \cdot trace\left[\left(\mathbf{F}^H\mathbf{F}\right)^{-1}\right]$$

Proving using the same method as with formula (6), which is not repeated here

$$E\left\{(\widehat{\sigma}_{LS} - \sigma)^2\right\} > \frac{o\left(\log\left(M\right)\right) \cdot S \cdot \sigma_x^2}{SNR \cdot L \cdot \left[1 + u_{LS}\left(S - 1\right)\right]}$$

Similarly, the bounds of sparsity defined as $S < \frac{1}{2}\left(\frac{1}{\bar{u}_{pr}} + 1\right)$ is applied, then

$$E\left\{(\widehat{\sigma}_{LS} - \sigma)^2\right\} > \frac{o\left(\log\left(M\right)\right) \cdot S \cdot \sigma_x^2}{SNR \cdot L \cdot \left[1 + 1/2 \cdot (1 - \bar{u}_{pr}) \cdot u_{LS}/\bar{u}_{pr}\right]} \quad (22)$$

APPENDIX II

Fig. 7 shows the imaging geometry of SAR. In this figure, the SAR sensor travels parallel to the y-axis and the velocity is V_e. η denotes a sampling instant ranged in the $[0, T_1]$ interval. H is the orbit height. Assuming that C is the tracking position of one sample, A and B are two point targets corresponding to two columns with maximum correlation in the reconstructed matrix $\mathbf{D}_{N \times M}$. R_0 is the nearest slant range between SAR
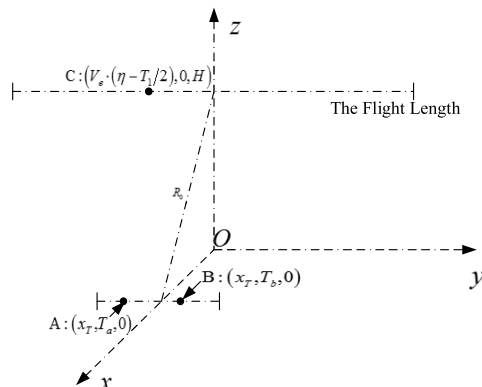
FIGURE 7. SAR imaging geometry.

and M point targets on the same nearest slant range. At the sampling instant η, two slant ranges between SAR sensor and point target A, and between SAR sensor and point target B are

$$R_a\left(\eta\right) = \sqrt{R_0^2 + (V_e \cdot (\eta - T_1/2) - T_a)^2}$$
$$\approx R_0 + \frac{(V_e \cdot (\eta - T_1/2) - T_a)^2}{2 \cdot R_0}$$
$$R_b\left(\eta\right) = \sqrt{R_0^2 + (V_e \cdot (\eta - T_1/2) - T_b)^2}$$
$$\approx R_0 + \frac{(V_e \cdot (\eta - T_1/2) - T_b)^2}{2 \cdot R_0},$$

respectively.

The mutual coherence coefficient u is denoted by the following:

$$u = \max_{1 \leq m1 \neq m2 \leq M} \frac{\left|\langle \mathbf{D}_i, \mathbf{D}_j \rangle\right|}{\|\mathbf{D}_i\|_2 \cdot \|\mathbf{D}_j\|_2}$$

$$= \frac{\left|\sum_{n=n_f}^{n_l} \exp\left\{j\frac{4\pi}{\lambda}\left(R_a\left(\eta_n\right) - R_b\left(\eta_n\right)\right)\right\}\right|}{\|\mathbf{D}_{m1}\|_2 \cdot \|\mathbf{D}_{m2}\|_2}$$

$$= \frac{\left|\sum_{n=n_f}^{n_l} \exp\left\{j\frac{2\pi}{\lambda R_0} \cdot \left[2V_e\left(\eta_n - \frac{T_1}{2}\right)(T_b - T_a) - \left(T_b^2 - T_a^2\right)\right]\right\}\right|}{\|\mathbf{D}_{m1}\|_2 \cdot \|\mathbf{D}_{m2}\|_2}$$

$$= \frac{\left|\sum_{n=n_f}^{n_l} \exp\left\{j\frac{4\pi \cdot V_e \eta_n \cdot (T_b - T_a)}{\lambda R_0}\right\}\right|}{\|\mathbf{D}_{m1}\|_2 \cdot \|\mathbf{D}_{m2}\|_2}$$
$$\cdot \left|\exp\left\{-j\frac{2\pi\left(T_b^2 - T_a^2 + V_e T_1 (T_b - T_a)\right)}{\lambda R_0}\right\}\right|$$

$$= \frac{\left|\sum_{n=n_f}^{n_l} \exp\left\{j\frac{4\pi \cdot V_e \eta_n \cdot (T_b - T_a)}{\lambda R_0}\right\}\right|}{\|\mathbf{D}_{m1}\|_2 \cdot \|\mathbf{D}_{m2}\|_2}$$

$$= \frac{\left|\sum_{n=n_f}^{n_l} \exp\left\{j\frac{4\pi \cdot V_e \eta_n \cdot |T_b - T_a|}{\lambda R_0}\right\}\right|}{\|\mathbf{D}_{m1}\|_2 \cdot \|\mathbf{D}_{m2}\|_2}, \quad (23)$$

Assume that d denotes the spacing $|T_b - T_a|$ between point target A and point target B. Based on the structure form of the reconstructed matrix $\mathbf{D}_{N \times M}$ in (3), the l_2-norm of each column is nearly equal, and assume that $||\mathbf{D}_i||_2 \approx L^2$. (23) is simplified to the following:

$$u = \frac{\left|\sum_{n=n_f}^{n_l} \exp\left\{j\frac{4\pi V_e d}{\lambda R_0} \eta_n\right\}\right|}{L^2} \quad (24)$$

When the mutual coherence is calculated in the random sub-Nyquist sampling method, the sampling instant η is a continuous random variable ranged in the $[0, T_1]$ interval, and assume that the probability density function of η is $p(\eta)$. Mean value $\bar{u}_r$ in the numerical characteristics of random

variable is used to analyse u_r:

$$
\begin{aligned}
&\bar{u}_{pr} \\
&= \max_{1 \le m1 \ne m1 \le M} \frac{|\langle \mathbf{D}_{m1}, \mathbf{D}_{m2}\rangle|}{\|\mathbf{D}_{m1}\|_2 \cdot \|\mathbf{D}_{m2}\|_2} \\
&= \frac{E\left(\left|\sum_{n=n_f}^{n_l} \exp\left\{j\frac{4\pi V_e d}{\lambda R_0}\eta_n\right\}\right|\right)}{L^2} \\
&= \frac{\underbrace{\int\!\!\int \cdots \int}_{\eta_n \in [0,T_1]}\left(\left|\sum_{n=n_f}^{n_l}\exp\left\{j\frac{4\pi V_e d}{\lambda R_0}\eta_n\right\}\right|\right.}{L^2} \\
&\quad \cdot \frac{\left. p\left(\eta_{n_f}, \eta_{(n_f+1)}, \cdots, \eta_{n_l}\right)\right) d\eta_{n_f}, d\eta_{(n_f+1)}, \cdots, d\eta_{n_l}}{L^2}
\end{aligned}
\tag{25}
$$

All the sampling instants are independent and identically distributed, so $p\left(\eta_{n_f}, \eta_{(n_f+1)}, \cdots, \eta_{n_l}\right) = p\left(\eta_{n_f}\right) \cdot p\left(\eta_{(n_f+1)}\right)\cdots p\left(\eta_{n_l}\right)$. Then

$$
\bar{u}_r = \frac{\underbrace{\int\!\!\int \cdots \int}_{\eta_n \in [0,T_1]}\left|\sum_{n=n_f}^{n_l}\exp\left\{j\frac{4\pi V_e d}{\lambda R_0}\eta_n\right\}\right|}{L^2}
\cdot \frac{p\left(\eta_{n_f}\right)p\left(\eta_{(n_f+1)}\right)\cdots p\left(\eta_{n_l}\right)d\eta_{n_f}d\eta_{(n_f+1)}\cdots d\eta_{n_l}}{L^2}
\tag{26}
$$

For this, the definite integral is transformed into the summation of infinite series, $\bar{u}_r$ in random sub-Nyquist sampling method is expressed as

$$
\bar{u}_r = \lim_{A\to\infty} \sum_{i_{n_f}=0}^{A}\sum_{i_{(n_f+1)}=0}^{A}
$$

$$
\cdots \sum_{i_{n_l}=0}^{A}\left(\left|\sum_{n=n_f}^{n_l}\exp\left\{j\frac{4\pi V_e d}{\lambda R_0}\left(\frac{i_n}{A}T_1\right)\right\}\right|\right.
$$
$$
\left. \cdot p\left(\frac{i_{n_f}}{A}T_1\right)\cdot p\left(\frac{i_{(n_f+1)}}{A}T_1\right)\cdots p\left(\frac{i_{n_l}}{A}T_1\right)\right.
$$
$$
\left. \cdot \frac{T_1}{A}\cdot\frac{T_1}{A}\cdot\ldots\cdot\frac{T_1}{A}\right)\bigg/ L^2.
\tag{27}
$$

When the mutual coherence is calculated in the pseudo-random sub-Nyquist sampling method, the sampling instant η is a discrete random variable and the set of all possible values as follows:

$$
\Omega = \left\{\frac{T_1}{N_{Nyquist}-1}\cdot 0, \frac{T_1}{N_{Nyquist}-1}\cdot 1, \cdots, \right.
$$
$$
\left. \frac{T_1}{N_{Nyquist}-1}\cdot(N_{Nyquist}-1)\right\},
$$

where $N_{Nyquist}$ is the number of samples in the Nyquist sampling method. Assuming that the probability of η is $f(\eta)$, mean value $\bar{u}_{pr}$ in the numerical characteristics of random variable is used to analyze u_{pr} (28), as shown at the bottom of this page, where each sampling instant η is independent and identically distributed, so

$$
f\left(\eta_{n_f}, \eta_{(n_f+1)}, \cdots, \eta_{n_l}\right) = f\left(\eta_{n_f}\right)\cdot f\left(\eta_{(n_f+1)}\right)\cdots f\left(\eta_{n_l}\right).
$$

In essence, the difference between random sub-Nyquist sampling method and pseudo-random sub-Nyquist sampling method is the sampling instant. The sampling instant of the former is a continuous random variable and that of the latter is a discrete random variable. To analyze the impact of different sampling methods on the mutual coherence, both should have the same distribution, e.g., if the former obeys a continuous Gaussian distribution with mean 0 and variance 1, the latter also should obey discrete Gaussian distribution with mean 0 and variance 1. Therefore, we set the following:

$$
f(\frac{i_n}{N_{\text{Nyquist}}-1}T_1) = \int_{\frac{T_1}{N_{\text{Nyquist}}}\cdot i_n}^{\frac{T_1}{N_{\text{Nyquist}}}\cdot(i_n+1)} p(\eta)d\eta \tag{29}
$$

$$
\begin{aligned}
\bar{u}_{pr} &= \max_{1\le m1\ne m1\le M}\frac{|\langle\mathbf{D}_{m1},\mathbf{D}_{m2}\rangle|}{\|\mathbf{D}_{m1}\|_2\cdot\|\mathbf{D}_{m2}\|_2} = \frac{E\left(\left|\sum_{n=n_f}^{n_l}\exp\left\{j\frac{4\pi V_e d}{\lambda R_0}\eta_n\right\}\right|\right)}{L^2} \\
&= \frac{\sum_{i_{n_f}=0}^{N_{Nyquist}-1}\sum_{i_{(n_f+1)}=0}^{N_{Nyquist}-1}\cdots\sum_{i_{n_l}=0}^{N_{Nyquist}-1}\left|\sum_{n=n_f}^{n_l}\exp\left\{j\frac{4\pi V_e d}{\lambda R_0}\eta_n\right\}\right|\cdot f(\eta_{n_f},\cdots,\eta_{n_l})}{L^2} \\
&= \sum_{i_{n_f}=0}^{N_{Nyquist}-1}\sum_{i_{(n_f+1)}=0}^{N_{Nyquist}-1}\cdots\sum_{i_{n_l}=0}^{N_{Nyquist}-1}\left(\left|\sum_{n=n_f}^{n_l}\exp\left\{j\frac{4\pi V_e d}{\lambda R_0}\cdot\left(\frac{i_n}{N_{Nyquist}-1}T_1\right)\right\}\right|\right. \\
&\quad \left. f(\frac{i_{n_f}}{N_{Nyquist}-1}T_1)\cdot f(\frac{i_{(n_f+1)}}{N_{Nyquist}-1}T_1)\cdots f(\frac{i_{n_l}}{N_{Nyquist}-1}T_1)\cdot\frac{T_1}{N_{Nyquist}}\cdot\frac{T_1}{N_{Nyquist}}\cdots\frac{T_1}{N_{Nyquist}}\right)\bigg/L^2.
\end{aligned}
\tag{28}
$$

Substituting (29) into (28), the equation (28) is simplified to the following:

$$
\begin{aligned}
&u_{pr}\\
&= \sum_{i_{n_f}=0}^{N_{Nyquist}-1} \sum_{i_{(n_f+1)}=0}^{N_{Nyquist}-1}\\
&\cdots \sum_{i_{n_l}=0}^{N_{Nyquist}-1} \left(\left| \sum_{n=n_f}^{n_l} \exp\left\{ j\frac{4\pi V_e d}{\lambda R_0} \cdot \left(\frac{i_n}{N_{Nyquist}-1} T_1 \right) \right\} \right| \right.\\
&\cdot \int_{\frac{T_1}{N_{Nyquist}}\cdot i_{n_f}}^{\frac{T_1}{N_{Nyquist}}\cdot(i_{n_f}+1)} p(\eta)d\eta \cdot \int_{\frac{T_1}{N_{Nyquist}}\cdot i_{(n_f+1)}}^{\frac{T_1}{N_{Nyquist}}\cdot(i_{(n_f+1)}+1)} p(\eta)d\eta\\
&\cdots \int_{\frac{T_1}{N_{Nyquist}}\cdot i_{n_l}}^{\frac{T_1}{N_{Nyquist}}\cdot(i_{n_l}+1)} p(\eta)d\eta \cdot \frac{T_1}{N_{Nyquist}} \cdot \frac{T_1}{N_{Nyquist}}\\
&\left. \cdots \frac{T_1}{N_{Nyquist}} \right) \bigg/ L^2
\end{aligned} \tag{30}
$$

For this, the sampling duration T_1 is very small and the number of Nyquist samples N_{Nyquist} is very large,

$$
\int_{\frac{T_1}{N_{Nyquist}}\cdot i_n}^{\frac{T_1}{N_{Nyquist}}\cdot(i_n+1)} p(\eta)d\eta \approx p\left(\frac{i_n}{N_{Nyquist}-1} \cdot T_1 \right) \cdot \frac{T_1}{N_{Nyquist}}. \tag{31}
$$

Then

$$
\begin{aligned}
&\bar{u}_{pr}\\
&= \sum_{i_{n_f}=0}^{N_{Nyquist}-1} \sum_{i_{(n_f+1)}=0}^{N_{Nyquist}-1}\\
&\cdots \sum_{i_{n_l}=0}^{N_{Nyquist}-1} \left(\left| \sum_{n=n_f}^{n_l} \exp\left\{ j\frac{4\pi V_e d}{\lambda R_0} \cdot \left(\frac{i_n}{N_{Nyquist}-1} T_1 \right) \right\} \right| \right.\\
&\cdot p\left(\frac{i_{n_f}}{N_{Nyquist}-1} \cdot T_1 \right) \cdot p\left(\frac{i_{(n_f+1)}}{N_{Nyquist}-1} \cdot T_1 \right)\\
&\cdots p\left(\frac{i_{n_l}}{N_{Nyquist}-1} \cdot T_1 \right)\\
&\left. \cdot \frac{T_1}{N_{Nyquist}} \cdot \frac{T_1}{N_{Nyquist}} \cdots \frac{T_1}{N_{Nyquist}} \right) \bigg/ L^2
\end{aligned} \tag{32}
$$

Comparing equation (27) with equation (32), $\bar{u}_r \approx \bar{u}_{pr}$ when the number of Nyquist samples N_{Nyquist} approaches infinity. In reality, N_{Nyquist} is much larger; therefore, we can assume that $\bar{u}_r \approx \bar{u}_{pr}$.

REFERENCES

[1] J. C. Curlander and R. N. McDonough, *Synthetic Aperture Radar: Systems and Signal Processing*. New York, NY, USA: Wiley, 1991.

[2] I. G. Cumming and F. H. Wong, *Digital Processing of Synthetic Aperture Radar Data: Algorithms and Implementation*. Norwood, MA, USA: Artech House, 2004.

[3] C. Oliver and S. Quegan, *Understanding Synthetic Aperture Radar Images*. Norwood, MA, USA: Artech House, 1998.

[4] D. Yang, G. Liao, S. Zhu, X. Yang, and X. Zhang, "SAR imaging with undersampled data via matrix completion," *IEEE Geosci. Remote Sens. Lett.*, vol. 11, no. 9, pp. 1539–1543, Sep. 2014.

[5] D. Takhar *et al.*, "A new compressive imaging camera architecture using optical-domain compression," *Proc. SPIE*, vol. 6065, p. 606509, Feb. 2006.

[6] C. Li, "An efficient algorithm for total variation regularization with applications to the single pixel camera and compressive sensing," M.S. thesis, Rice Univ., Houston, TX, USA, Sep. 2009.

[7] M.-A. Petrovici, C. Damian, C. Udrea, F. Garoi, and D. Coltuc, "Single pixel camera with compressive sensing by non-uniform sampling," in *Proc. Int. Conf. Commun.*, Jun. 2016, pp. 443–448.

[8] J. A. Tropp, J. N. Laska, M. F. Duarte, J. K. Romberg, and R. G. Baraniuk, "Beyond Nyquist: Efficient sampling of sparse bandlimited signals," *IEEE Trans. Inf. Theory*, vol. 56, no. 1, pp. 520–544, Jan. 2010.

[9] M. Mishali and Y. C. Eldar, "From theory to practice: Sub-Nyquist sampling of sparse wideband analog signals," *IEEE J. Sel. Topics Signal Process.*, vol. 4, no. 2, pp. 375–391, Apr. 2010.

[10] E. Matusiak and Y. C. Eldar, "Sub-Nyquist sampling of short pulses," *IEEE Trans. Signal Process.*, vol. 60, no. 3, pp. 1134–1148, Mar. 2012.

[11] H. Zhao, J. Zhang, L. Qiao, and Y. Chen, "A multichannel compressed sampling method for fractional bandlimited signals," *Signal Process.*, vol. 134, pp. 139–148, May 2017.

[12] K. Aberman and Y. C. Eldar, "Sub-Nyquist SAR via Fourier domain range-Doppler processing," *IEEE Trans. Geosci. Remote Sens.*, vol. 55, no. 11, pp. 6228–6244, Nov. 2017.

[13] C. Herley and P. W. Wong, "Minimum rate sampling and reconstruction of signals with arbitrary frequency support," *IEEE Trans. Inf. Theory*, vol. 45, no. 5, pp. 1555–1564, Jul. 1999.

[14] Y. Ma, Y. Gao, Y.-C. Liang, and S. Cui, "Reliable and efficient sub-Nyquist wideband spectrum sensing in cooperative cognitive radio networks," *IEEE J. Sel. Areas Commun.*, vol. 34, no. 10, pp. 2750–2762, Oct. 2016.

[15] P. D. Hale, C. M. Wang, D. F. Williams, K. A. Remley, and J. D. Wepman, "Compensation of random and systematic timing errors in sampling oscilloscopes," *IEEE Trans. Instrum. Meas.*, vol. 55, no. 6, pp. 2146–2154, Dec. 2006.

[16] M. O. Sonnaillon, R. Urteaga, and F. J. Bonetto, "High-frequency digital lock-in amplifier using random sampling," *IEEE Trans. Instrum. Meas.*, vol. 57, no. 3, pp. 616–621, Mar. 2008.

[17] Y. Zhao and J. Liu, "Sequential time interleaved random equivalent sampling for repetitive signal," *Rev. Sci. Instrum.*, vol. 87, no. 12, p. 125106, Oct. 2016.

[18] M. T. Alonso, P. López-Dekker, and J. J. Mallorquí, "A novel strategy for radar imaging based on compressive sensing," *IEEE Trans. Geosci. Remote Sens.*, vol. 48, no. 12, pp. 4285–4295, Dec. 2011.

[19] S. Ji, Y. Xue, and L. Carin, "Bayesian compressive sensing," *IEEE Trans. Signal Process.*, vol. 56, no. 6, pp. 2346–2356, Jun. 2008.

[20] G. Golub and C. F. van Loan, *Matrix Computations*, 3rd ed. Baltimore, MD, USA: The Johns Hopkins Univ. Press, 1996.

[21] S. D. Babacan, R. Molina, and A. K. Katsaggelos, "Bayesian compressive sensing using Laplace priors," *IEEE Trans. Image Process.*, vol. 19, no. 1, pp. 53–63, Jan. 2010.

[22] D. P. Wipf and B. D. Rao, "Sparse Bayesian learning for basis selection," *IEEE Trans. Signal Process.*, vol. 52, no. 8, pp. 2153–2164, Aug. 2004.

[23] E. E. Kuruoglu and J. Zerubia, "Modeling SAR images with a generalization of the Rayleigh distribution," *IEEE Trans. Image Process.*, vol. 13, no. 4, pp. 527–533, Apr. 2004.

[24] K. Sarabandi, "Derivation of phase statistics from the Mueller matrix," *Radio Sci.*, vol. 27, no. 5, pp. 553–560, Sep./Oct. 1992.

[25] J. A. Kong, A. A. Swartz, H. A. Yueh, L. M. Novak, and R. T. Shin, "Identification of terrain cover using the optimum polarimetric classifier," *J. Electromagn. Waves Appl.*, vol. 2, no. 2, pp. 171–194, 1987.

[26] E. J. Candès and T. Tao, "Decoding by linear programming," *IEEE Trans. Inf. Theory*, vol. 51, no. 12, pp. 4203–4215, Dec. 2005.

[27] J. Romberg, "Compressive sensing by random convolution," *SIAM J. Imag. Sci.*, vol. 2, no. 4, pp. 1098–1128, 2009.

[28] F. Alonso and M. Santos, "Ga optimization of the height of a low Earth orbit," in *Computational Intelligence in Decision and Control*. Singapore: World Scientific, 2008, pp. 719–724.

[29] A. Currie and M. A. Brown, "Wide-swath SAR," *IEE Proc. F Radar Signal Process.*, vol. 139, no. 2, pp. 122–135, Apr. 1992.

[30] F. De Zan and A. M. Guarnieri, "TOPSAR: Terrain observation by progressive scans," *IEEE Trans. Geosci. Remote Sens.*, vol. 44, no. 9, pp. 2352–2360, Sep. 2006.

[31] L. M. H. Ulander, H. Hellsten, and G. Stenström, "Synthetic-aperture radar processing using fast factorized back-projection," *IEEE Trans. Aerosp. Electron. Syst.*, vol. 39, no. 3, pp. 760–776, Jul. 2003.

[32] P. Snoeij *et al.*, "Sentinel-1 radar mission: Status and performance," *IEEE Aerosp. Electron. Syst. Mag.*, vol. 25, no. 8, pp. 32–39, Aug. 2010.

[33] H. L. Van Trees, K. L. Bell, and Z. Tian, *Detection Estimation and Modulation Theory: Part I: Detection, Estimation, and Filtering Theory*, 2nd ed. Hoboken, NJ, USA: Wiley, 2013.

[34] Z. Ben-Haim, Y. C. Eldar, and M. Elad, "Coherence-based performance guarantees for estimating a sparse vector under random noise," *IEEE Trans. Signal Process.*, vol. 58, no. 10, pp. 5030–5043, Oct. 2010.

[35] E. J. Candès and T. Tao, "The Dantzig selector: Statistical estimation when p is much larger than n," *Ann. Statist.*, vol. 35, no. 6, pp. 2313–2351, 2007.

[36] T. T. Cai, L. Wang, and G. Xu, "Stable recovery of sparse signals and an oracle inequality," *IEEE Trans. Inf. Theory*, vol. 56, no. 7, pp. 3516–3522, Jul. 2010.

WENJIAO CHEN was born in Anyang, Henan, China, in 1991. She is currently pursuing the Ph.D. degree in electronics engineering with Beihang University.

Her research interests include system design and signal processing for a wide-swath synthetic aperture radar, as well as system performance analysis for an aperture radar.

PENG XIAO was born in Harbin, Heilongjiang, China, in 1984. He received the B.S. degree in communication engineering and a Ph.D. degree in communication and information systems from Beihang University, Beijing, China, in 2007 and 2014, respectively.

From 2014 to 2017, he held a post-doctoral position with Beihang University. Since 2017, he has been a Research Assistant with the Qian Xuesen Laboratory of Space Technology, China Academy of Space Technology, Beijing. His research interests include innovative remote sensing systems and applications based on ultra-wide-swath imaging with synthetic aperture radar systems, multistatic satellite formations, and the development of advanced signal algorithms.

ZE YU (M'13) was born in Xi'an, Shanxi, China, in 1979. He received the B.S. degree in electronics engineering and the Ph.D. degree in communication and information systems from Beihang University, Beijing, China, in 2002 and 2007, respectively.

Since 2009, he has been with the School of Electronics and Information Engineering, Beihang University. He is currently involved in the system design and imaging processing for a high-resolution and wide-swath synthetic aperture radar.

CHUNSHENG LI received the Ph.D. degree in signal and information processing from Beihang University, Beijing, China, in 1998.

Since 2005, he has been a Professor with the School of Electronics and Information Engineering, Beihang University. He has authored over 100 journal and conference papers and four books. His research interests include analysis and simulation of synthetic aperture radar satellites, high-resolution image formation, and multimodal remote sensing data fusion.

● ● ●